Fault kinematics and surface deformation across a releasing bend during the 2010 M_W 7.1 Darfield, New Zealand, earthquake revealed by differential LiDAR and cadastral surveying

Brendan Duffy[1,†], Mark Quigley[1], David J.A. Barrell[2]; Russ Van Dissen[2], Timothy Stahl[1], Sébastien Leprince[3], Craig McInnes[4], and Eric Bilderback[1]

[1]*Department of Geological Sciences, University of Canterbury, Private Bag 4800, Christchurch 8140, New Zealand*

[2]*GNS Science, PO Box 30-368, Lower Hutt 5040, New Zealand*

[3]*Division of Geological and Planetary Sciences, California Institute of Technology, MC 170-25 1200 E. California Blvd., Pasadena, California 91125, USA*

[4]*Fox and Associates–Consulting Surveyors, 333 Harewood Road, Christchurch 8053, New Zealand*

ABSTRACT

Dextral slip at the western end of the east-west–striking Greendale fault during the 2010 M_W 7.1 Darfield earthquake transferred onto a northwest-trending segment, across an apparent transtensional zone, here named the Waterford releasing bend. We used detailed surface mapping, differential analysis of pre- and postearthquake light detection and ranging (LiDAR), and property boundary (cadastral) resurveying to produce high-resolution (centimeter-scale) estimates of coseismic ground-surface displacements across the Waterford releasing bend. Our results indicate that the change in orientation on the Greendale fault incorporates elements of a large-scale releasing bend (from the viewpoint of westward motion on the south side of the fault) as well as a smaller-scale restraining stepover (from the viewpoint of southeastward motion on the north side of the fault). These factors result in the Waterford releasing bend exhibiting a decrease in displacement to near zero at the change in strike, and the presence within the overall releasing bend of a nested, localized restraining stepover with contractional bulging. The exceptional detail of surface deformation and kinematics obtained from this contemporary surface-rupture event illustrates the value of multimethod investigations. Our data provide insights into strike-slip fault bend kinematics, and into the potentially subtle but important structures that may be present at bends on historic and prehistoric rupture traces.

[†]E-mail: brendan.duffy@canterbury.ac.nz

INTRODUCTION

Over the past 10 years or so, documentation of earthquake fault surface rupture by well-established field methods, including geological/geomorphological mapping and geodetic surveying, has increasingly been supplemented by technologies such as interferometric synthetic aperture radar (InSAR) (e.g., Reigber et al., 1997; Price and Burgmann, 2002; Beavan et al., 2010a) and light detection and ranging (LiDAR) (e.g., Hudnut et al., 2002; Quigley et al., 2012). In combination, these methods provide an opportunity to examine fault deformation and kinematics in unrivaled detail and precision. Contemporary surface-rupture events, in favorable land-surface settings, provide primary evidence for the style and kinematics of fault deformation, and documentation of their character provides an invaluable interpretive analogue for structural and kinematic studies of prehistoric fault deformation.

The 2010 Darfield earthquake in Canterbury, New Zealand (Fig. 1), caused surface rupture of the Greendale fault across a low-relief alluvial plain. The plain is an intensively farmed agricultural region and contains a multitude of straight lines in the form of roads, fences, and ditches that provided ideal piercing points for quantifying fault rupture (Barrell et al., 2011; Quigley et al., 2012; Villamor et al., 2012). Quigley et al. (2012) took advantage of these piercing points to undertake detailed field mapping and, in combination with evaluation of LiDAR flown after the earthquake, were able to quantify fault offsets to high precision. Serendipitously, two high-quality geodetic data sets had been acquired prior to the earthquake, in the vicinity of the western end of the Greendale fault. A LiDAR survey flown 5 months before the earthquake was partly overlapped by LiDAR flown a few days after the earthquake. Also, a cadastral survey was conducted 1 month before the earthquake on a property through which the Greendale fault subsequently ruptured for ~2 km. Rupture of the Greendale fault also temporarily diverted the course of the Hororata River. In this study, we mapped the earthquake-induced flood, analyzed pre- and postearthquake LiDAR surveys, and undertook postearthquake cadastral resurveying of property boundaries, to further aid understanding of the surface deformation and displacement across the Greendale fault. These data sets span a zone where the fault strike changed by ~40°, and they have allowed us to characterize this fault bend in remarkable detail. Documentation of this detail is the focus of this paper.

THE DARFIELD EARTHQUAKE

New Zealand lies astride the boundary between the Pacific and Australian plates, at a location where they converge obliquely at rates of 30–50 mm/yr (DeMets et al., 2010) (Fig. 1A). Continental collision across the South Island drives uplift of the Southern Alps (Norris and Cooper, 2001) and is expressed by varying rates and styles of active deformation across Canterbury (Pettinga et al., 2001; Campbell et al., 2012). The rupture of a fault network beneath the Canterbury Plains, eastern South Island, on 4 September 2010 generated the M_W 7.1 Darfield earthquake (Beavan et al., 2010b; Gledhill et al., 2010, 2011; Beavan et al., 2012), which caused widespread ground shaking and damage (Cubrinovski et al., 2010; Gledhill et al., 2010; Quigley et al., 2010a, 2010b, 2013;

GSA Bulletin; March/April 2013; v. 125; no. 3/4; p. 420–431; doi: 10.1130/B30753.1; 7 figures; 3 tables.

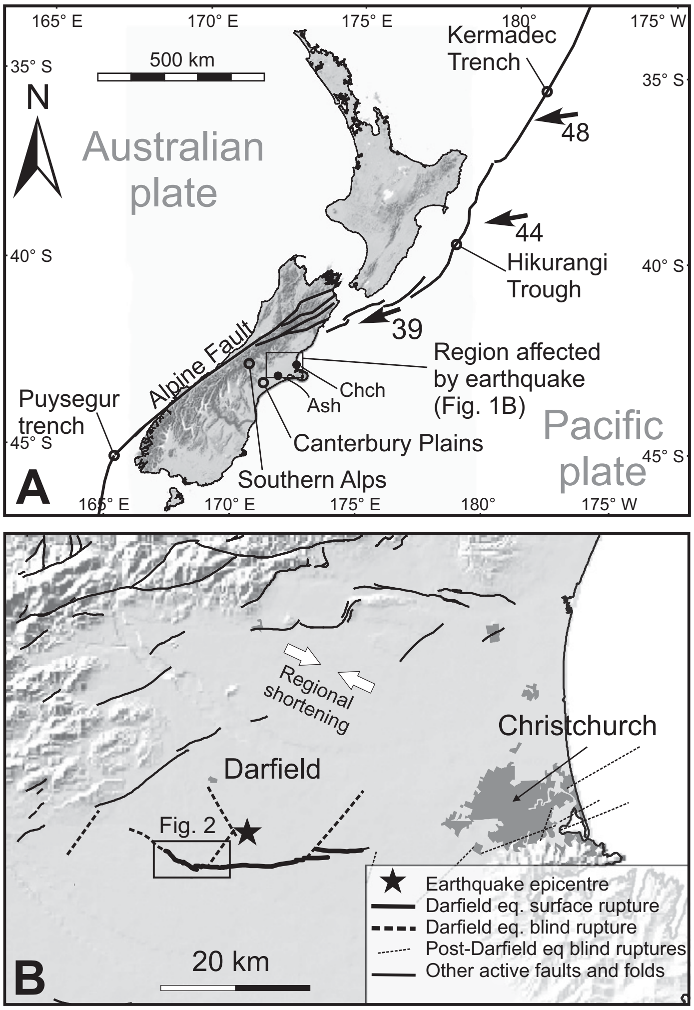

Figure 1. Regional setting. (A) New Zealand plate boundary and relative motion vectors (mm/yr) between the Australian and Pacific plates (DeMets et al., 2010). Canterbury Plains form the low relief east of the Southern Alps in the central South Island. Ash—Ashburton; Chch—Christchurch. (B) Location of the Greendale fault west of Christchurch in mid-Canterbury. The extent of surface rupture is from Quigley et al. (2012), and extents of blind ruptures are from Beavan et al. (2012). Known active (i.e., late Quaternary) faults and folds are based on GNS Science QMAP data sets (Cox and Barrell, 2007; Forsyth et al., 2008). Regional shortening direction is from Sibson et al. (2011).

Van Dissen et al., 2011). Geodetic modeling has revealed that this single earthquake event consisted of an interlinked succession of ruptures on several fault structures (Figs. 1B and 2) (Beavan et al., 2012). All remained blind, apart from the Greendale fault, which produced an ~30-km-long surface rupture, predominantly strike slip with dextral sense (Quigley et al., 2010a, 2010b, 2012; Barrell et al., 2011). The Greendale fault lies in a large sedimentary basin. Fault rupture was initiated ~10 km deep, within indurated, slightly metamorphosed, Mesozoic graywacke rock, and propagated to the surface through a surficial 1–1.5-km-thick cover of post–mid-Cretaceous sedimentary strata, including as much as 500 m of Quaternary fluvial gravels (Browne et al., 2012; Jongens et al., 2012).

The Greendale fault is composed of three geometric segments, each named for their relative locations (Quigley et al., 2012). The East and Central segments strike east-west, whereas the West segment strikes northwest (Fig. 2). In the context of dextral rupture exhibited by the fault trace, the strike change between the West and Central segments is transtensional in nature (Quigley et al., 2012), so the zone across which the strike change occurs is referred to here as the Waterford releasing bend, taking its name from a nearby farm. Dextral displacement of up to ~5.3 m on the Central segment decreases to ~1.2 m on the West segment (Quigley et al., 2012). The West segment displayed a notably south-side-up vertical component of offset (~1.5 m), which caused temporary partial avulsion of the Hororata River (Quigley et al., 2010b; Barrell et al., 2011) (Fig. 2). Seismic source models indicate that the Greendale fault rupture proceeded bilaterally from the vicinity of the Waterford releasing bend, which itself lies close to the intersection of the Greendale fault with the northeast-southwest–striking Charing Cross reverse fault, on which the Darfield earthquake was initiated (Fig. 2) (Holden et al., 2011; Beavan et al., 2012).

METHODS

Flood Mapping

We mapped the extent of avulsion-induced postearthquake flooding (Figs. 2 and 3) by digitizing flooded areas seen in a set of overlapping oblique aerial photographs taken ~12 h after the earthquake. We georeferenced the photographs using ArcGIS software with reference to digital topographic maps and pre-earthquake digital orthophotos.

Cadastral Surveys

Cadastral surveys have been used to document surface displacements resulting from the Chi-Chi earthquake in Taiwan (Lee et al., 2006, 2010, 2011). A cadastral property survey done about 1 month before the earthquake in New Zealand spanned the northern half of the West segment of the Greendale fault. Baseline surveying employed a Trimble R8 Global Navigation Satellite System (GNSS) real-time kinematic (RTK), and the survey was adjusted in "12d Model" software using simple loops and the Bowditch adjustment method (Bowditch, 1808). The survey was fixed relative to local benchmarks by locating the RTK base station on a buried iron tube witness mark that was established relative to three local benchmarks in 2004. The flat, unforested farmland provided a favorable global positioning system (GPS) environment, so the baseline survey over the survey extent of 2 km is likely to be internally accurate to within 2 cm, with exact accuracy depending on the detail of satellite geometry during the survey (Table 1).

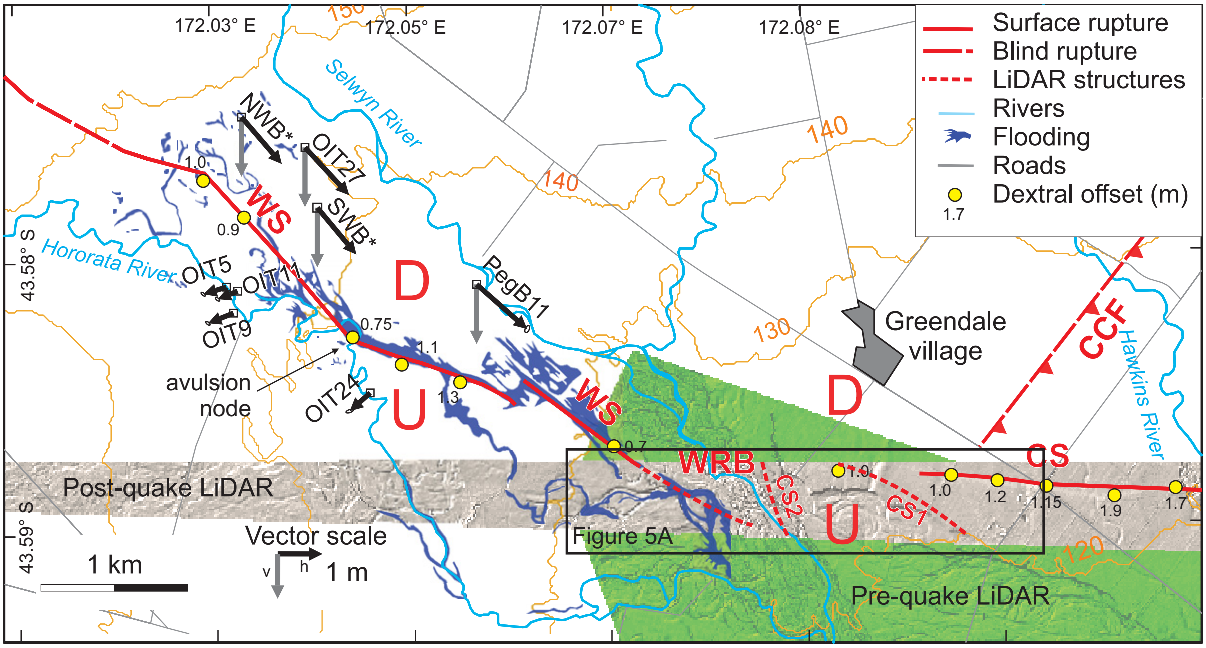

Figure 2. Fault map of the West segment (WS) and westernmost part of the Central segment (CS) of the Greendale fault. U and D denote relative upthrow and downthrow across the scarp. The immediate area of the change in strike between the segments is here named the Waterford releasing bend (WRB). CCF is the location of the subsurface tip of the blind Charing Cross fault (Beavan et al., 2012), teeth toward hanging wall. The extent of coseismic avulsion and resulting flooding is shown, as well as the location of pre- and postearthquake light detection and ranging (LiDAR). Arrows indicate displacement vectors for resurveyed cadastral witness marks (Table 2). Dotted red lines denote structures defined from LiDAR analysis in this study (Fig. 5). Dextral offset measurements are from Quigley et al. (2012). The Waterford releasing bend includes an ~1.5-km-wide zone where no surface deformation was able to be detected from field mapping. Topographic contours (brown) are in meters above sea level. Contours, roads, and streams are from Land Information NZ digital data, Crown Copyright reserved (used with permission). OIT—old iron tube; NWB—NW boundary peg; SWB—SW boundary peg.

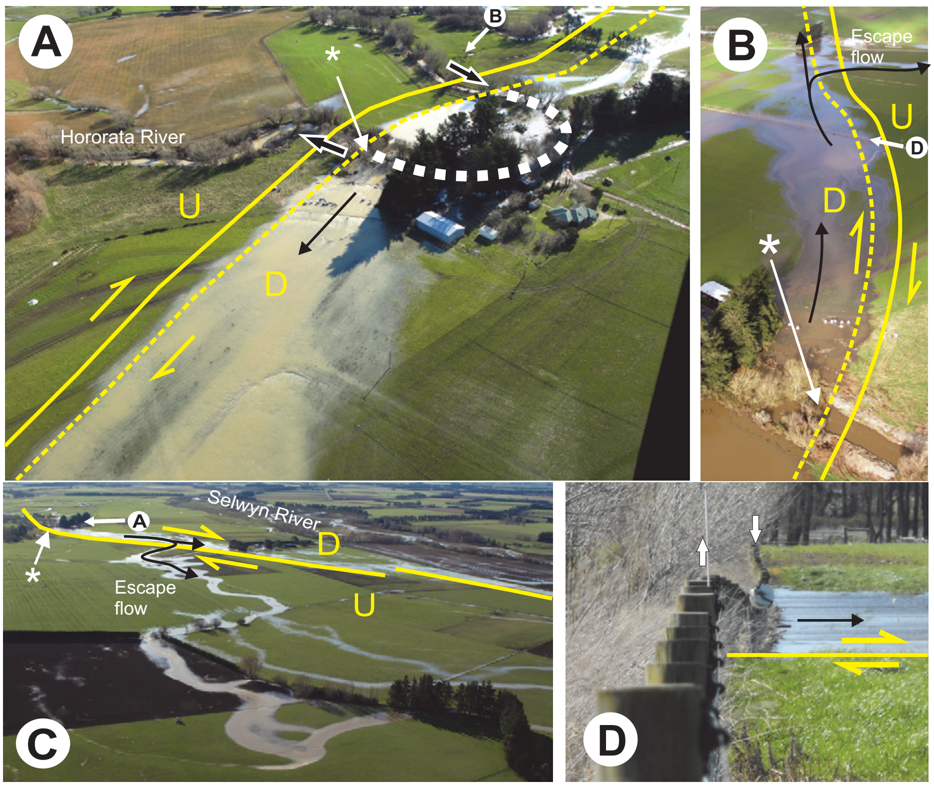

Figure 3. Deformation and flooding resulting from rupture of the West segment of the Greendale fault. Solid line and dashed line mark the crest and base of the surface trace, respectively, while U and D denote relative upthrow and downthrow. Thin black arrows show the direction of avulsion flow. (A) View to the northwest of the avulsion node (*) (Barrell et al., 2011). Here, ~1.5 m of oblique dextral southwest-side-up displacement impeded the Hororata River channel (dashed white), leading to partial avulsion and widespread flooding. Block arrows show original flow direction. Large shed is 20 m long. (B) View to the southeast from the avulsion node showing scarp-parallel flooding and escape flow across the scarp via a preexisting channel on the alluvial plain. Location/orientation of photo is indicated on A. (C) Long view north showing the split of the flooding due to southward escape from the scarp-directed flow. (D) View northeast across the scarp, showing relationship of flooding to dextral and vertical deformation of previously straight fence line (location indicated by white arrows). Location/orientation of photo is indicated on photo in B.

After the Darfield earthquake, we re-occupied 13 of the cadastral survey marks lying within 200–700 m of the West segment rupture trace (Table 2). The ground-surface positions of two boundary pegs (NWB and SWB; Fig. 2) were established in the IGS05 reference frame by a 24-h-mode GPS survey on 14–15 April 2011, 7 months after the Darfield earthquake. Both marks lie northeast of the surface rupture, so a correction was applied to remove the effects of postseismic deformation, based on trends observed during repeat observations of nearby first-order benchmarks a few kilometers north of the fault (Beavan et al., 2012). The corrected observations were converted to NZGD2000, then to the NZGD2000 Mount Pleasant Circuit coordinate system, and then finally to New Zealand Map Grid (NZMG), replicating transformations applied to the pre-earthquake cadastral survey. Taking account of the various error sources, the accuracy of ground-surface displacements of these marks is likely to be ±5 cm (John Beavan, 2011, GNS Science, personal commun.; Table 1).

We resurveyed the cadastral marks using a Trimble 5600 semirobotic total station and reduced the data using Trimble's Terramodel 10.41 survey software. We georeferenced the total station survey by assigning the GPS survey coordinates to pegs NWB and SWB. Pre- and postearthquake surveys were combined in a single AutoCAD drawing, and point displacements were measured in terms of azimuth and horizontal (Table 2) and vertical components (Table 3; Figs. 2 and 4).

LiDAR

Aerial LiDAR surveys provide high-resolution topographic data using the two-way travel-time of laser pulses. Such data sets are used to image fault scarps in a variety of environments (Hudnut et al., 2002; Muller and Harding, 2007). In this study, we documented the vertical motions associated with uplift and subsidence in the Waterford releasing bend area by differencing pre- and postearthquake LiDAR data where they overlapped (see Fig. 2). This technique has been widely applied in a diverse range of earth science disciplines, including volcanology (Marsella et al., 2009) and glaciology, and has recently been applied to fault surface rupture (Oskin et al., 2012).

Two LiDAR data sets were collected in 2010 using NZ Aerial Mapping's (NZAM) Optech ALTM 3100EA LiDAR system with system PRF set to 70 KHz. Pre-earthquake LiDAR was flown in late March 2010 at 1300 m above ground with a 40° field of view. The pre-earthquake survey was controlled using a geodetic reference mark established by NZAM at Ashburton (Fig. 1A), and positional and vertical accuracy was verified by an independent commercial survey. Vertical accuracy for ground returns in the Selwyn area was 0.07 m (1σ) across five sites (Table 1). NZAM checked the positional accuracy using surveyed positions of vertical discontinuities such as bridges and walls and found it to be a good fit. The LiDAR data were supplied for this project as a 1 m pixel raster.

Postearthquake LiDAR was flown along the general line of the Greendale fault on 10 September 2010 at 600 m above ground, with a field of view of 38°, but it did not encompass the West segment because it had not, at that time, been delineated by mapping. This LiDAR survey was brought into terms of the postearthquake geodetic reference system using a control site established by GNS Science. Vertical accuracy of ground returns was determined using the GNS control site and adjusted to improve it from an average height difference of ±0.03 m to 0.00 m (Table 1). Positional accuracy was checked by overlaying GNS Science survey data over LiDAR data, and a good fit was observed. Postearthquake LiDAR data were supplied for this project as a 0.5 m pixel raster.

Overlapping pre-earthquake LiDAR was subtracted from the postearthquake LiDAR, and the difference was mapped at 1 m cell size, the resolution of the pre-earthquake LiDAR raster (Fig. 5). Subpixel correlation of the pre- and postearthquake LiDAR rasters was carried out using COSI-Corr to determine horizontal offsets (Leprince et al., 2007a, 2007b; Konca et al., 2010).

DEFORMATION AND KINEMATICS OF SURFACE RUPTURE

Coseismic Scarp Development and Avulsion

As a result of the earthquake, the West segment of the Greendale fault formed a coseismic scarp across a meander bend in the Hororata River (Figs. 2 and 3A). The scarp impeded downstream flow and partly avulsed the Hororata River onto an older, higher surface. The river flow was high and relatively turbid, resulting from the expulsion of large volumes of groundwater as a result of the earthquake. Within 2 km of the fault trace, the unconfined groundwater table rose by several tens of meters (Cox et al., 2012), producing widespread uncontrolled artesian flows from bores and from earthquake-induced ground fissures. During field mapping, we observed numerous examples of fissures, surrounded by localized deposits of sand and fine-gravel ejecta, which attest to the force of the groundwater expulsion.

The newly formed scarp directed part of the Hororata River flow to the southeast (Fig. 2), parallel to and generally within 100 m of the scarp (Fig. 3). Fortunately, the avulsion flooding was identified from the air and recorded photographically within 12 h of the rupture, because the landowners moved rapidly to remediate the flooding by deepening the bed of the Hororata River across the scarp. Documentation of the onlap of avulsion floodwater along the scarp was instrumental in defining the location of the West segment, and guiding the field mapping of displacements (Fig. 3D). Mapping of the distribution of floodwaters from georeferenced oblique aerial photographs revealed subtle features such as slight strike changes and the presence of a small left stepover (Fig. 2).

Kinematics of the West Segment of the Greendale Fault

Barrell et al. (2011) and Quigley et al. (2012) reported that much of the dextral displacement, especially on the East segment, was accommodated by horizontal flexure that was mappable only with reference to previously linear features. The West segment scarp was rounded rather than sharp, and involved displacement of the order of 1 m, distributed over a zone typically ~20 m wide (Fig. 3D). No free faces were observed on the West segment, which suggests that ground-surface deformation was an oblique-dextral monoclinal flexure of near-surface gravelly sediments above the fault plane (Fig. 4).

Cadastral survey marks show a distinct pattern of displacement relative to the West segment of the fault. On each side of the fault, the

TABLE 1. ESTIMATED ACCURACY OF DATA USED IN DETERMINATION OF SURFACE DISPLACEMENTS

	Horizontal (m)		Vertical (m)	
Survey	IGS05	Relative	Lyttelton (1937) *in* NZGeoid05	Relative
Pre-earthquake cadastral	±0.05	±0.02	NA	±0.02
Postearthquake GPS	±0.05	0		
Postearthquake cadastral	*	0 < 0.16	NA	±0.15
Pre-earthquake light detection and ranging (LiDAR)		<0.1†	0.07	
Postearthquake LiDAR		<0.1†	0	

*Sum of postearthquake global positioning system (GPS) and error ellipse dimensions from Table 2.
†Based on COSI-Corr results.

TABLE 2. WATERFORD FARM TRILATERATION NETWORK LOCATIONS AND SHIFTs

Point ID	Error ellipses			Pre-earthquake		Postearthquake		Shifts			
	Major axis (m)	Minor axis (m)	Azimuth	Easting	Northing	Easting	Northing	Easting	Northing	Magnitude	Azimuth
Hanging wall											
OIT 28	0.074	0.030	308°57′18″	2432259.755	5736862.809	2432260.741	5736861.735	0.986	−1.074	1.458	137.433
NWB	Fixed with GPS survey	0.000	0.000	2432144.186	5736738.788	2432145.117	5736737.705	0.931	−1.083	1.428	139.308
OIT 27	0.074	0.030	308°57′18″	2432579.007	5736523.240	2432580.008	5736522.193	1.000	−1.047	1.448	136.307
OPEG 48	0.022	0.019	310°07′45″	2432779.314	5736217.303	2432780.285	5736216.250	0.971	−1.053	1.433	137.337
SWB	Fixed with GPS survey	0.000	0.000	2432664.006	5736120.018	2432664.882	5736118.971	0.875	−1.047	1.365	140.112
PEG B11	0.144	0.024	64°42′50″	2433753.819	5735597.614	2433755.013	5735596.558	1.194	−1.056	1.594	131.499
Footwall											
OPEG 47	0.108	0.016	311°26′44″	2432054.014	5735579.074	2432053.522	5735578.894	−0.493	−0.180	0.525	249.980
OIT 5	0.115	0.021	310°49′56″	2432020.894	5735552.382	2432020.370	5735552.204	−0.524	−0.178	0.554	251.225
OIT 11	0.105	0.016	316°33′07″	2432121.319	5735543.383	2432120.900	5735543.212	−0.418	−0.171	0.452	247.822
OIT 9	0.119	0.025	320°49′52″	2432116.744	5735410.867	2432116.185	5735410.675	−0.560	−0.192	0.591	251.099
OPEG 41	0.121	0.026	319°58′16″	2432097.694	5735401.008	2432097.075	5735400.764	−0.619	−0.245	0.665	248.416
OIT 24	0.160	0.045	14°01′38″	2433027.352	5734858.853	2433026.901	5734858.433	−0.451	−0.421	0.616	226.973
OLD POST	0.163	0.045	14°29′41″	2433036.960	5734832.804	2433036.502	5734832.378	−0.457	−0.426	0.625	227.037
Average hanging wall								0.993	−1.060	1.454	136.999
1σ deviation hanging wall								0.108	0.015	0.076	3.035
Average footwall								−0.505	−0.272	0.584	242.095
1σ deviation footwall								0.076	0.120	0.074	11.770

Note: Coordinates are in New Zealand Map Grid coordinate system. All values are in meters, except azimuth, which is in degrees. Data are grouped to show marks on the hanging wall (direction E) ordered from north to south, followed by marks on the footwall (direction SW), also ordered north to south. OIT—old iron tube; NWB—NW boundary peg; OPEG—old peg; SWB—SW boundary peg.

marks showed only small amounts of vertical movement relative to one another (average of ~0.12 m), but the marks on one side of the fault shifted substantially and consistently relative to those on the other side (Table 3). On the northeast side of the fault, marks were downthrown by an average of 1.48 m (maximum 1.6 m) relative to OIT11, the survey mark on the southwest side of the fault closest to the fault trace (Fig. 2; Table 3). The northeast side of the fault moved horizontally an average of 1.45 m toward 137° (maximum 1.59 m toward 131.5°) (Fig. 2; Table 2); these vectors are approximately parallel to the strike of the fault. The southwest side of the fault moved horizontally an average of 0.58 m toward 242° (maximum 0.67 m toward 248.5°); these vectors are approximately perpendicular to and away from the fault trace, and thus perpendicular to displacement on the downthrown side. These observations indicate that the West segment fault is extensional and may therefore be robustly inferred to dip toward the northeast.

The flexural nature of the scarp means that the West segment fault plane is not exposed, so we used the cadastral survey displacements to estimate the fault-plane attitude and the orientation and magnitude of the net slip on the fault (Fig. 4). The fault scarp through most of the cadastral survey area strikes 138°. The horizontal displacements of the upthrown and downthrown sides were applied in their displacement directions and yielded an average horizontal component of net slip of 1.7 m toward 117.7° (maximum of 1.99 m toward 114°). Adding the vertical displacement between the southwest and northeast sides of the fault to the horizontal slip returns an average net slip of 2.25 m (maximum 2.55 m) (Fig. 4) on a fault dipping ~68° to the northeast (63° using maximum slip values). For both average and maximum calculations, the net slip rakes 45° from the south, which yields a transtensional dip-slip to strike-slip ratio of 1:1.

Kinematics of the Waterford Releasing Bend

Differencing of the two 2010 LiDAR surveys reveals the displacement patterns across the Waterford releasing bend between the West and Central segments (Fig. 5A). The difference map has negative elevation values for subsidence and positive values for uplift. We note that vertical differences can arise from horizontal as well as vertical displacement of topographic features (e.g., Mukoyama, 2011; Oskin et al., 2012). Within Figure 5A, bright vertical anomalies denote horizontal displacement of the margins of streams and abandoned channels, as well as braid channels of the Selwyn River that have

TABLE 3. RELATIVE ELEVATION CHANGE MATRIX FOR CADASTRAL MARKS

	Height adjustments	OIT28	OIT27	OPEG 48	PEG B11	OPEG 47	OIT 5	OIT 11	OIT 9	OPEG 41	OIT 24
OIT28	Open	0	0.2156	0.1065	0.0819	–1.131	–0.9837	–1.3831	–1.2316	–1.0466	–1.1746
OIT27	0.173		0	–0.1091	–0.1337	–1.3466	–1.1993	–1.5987	–1.4472	–1.2622	–1.3902
OPEG 48	0			0	–0.0246	–1.2375	–1.0902	–1.4896	–1.3381	–1.1531	–1.2811
PEG B11	0.119		Hanging wall		0	–1.2129	–1.0656	–1.465	–1.3135	–1.1285	–1.2565
OPEG 47	0.071					0	0.1473	–0.2521	–0.1006	0.0844	–0.0436
OIT 5	0.113						0	–0.3994	–0.2479	–0.0629	–0.1909
OIT 11	0.102							0	0.1515	0.3365	0.2085
OIT 9	0.113								0	0.185	0.057
OPEG 41	0.113									0	–0.128
OIT 24	0.173						Footwall				0

Note: Negative values indicate that the mark listed in the row has subsided relative to the mark listed in the column. OIT—old iron tube; OPEG—old peg.

migrated during the interval between the surveys. However, due to the subdued topography within the study area, this latter effect is insignificant compared with tectonic displacements.

The differential elevation map (Fig. 5A) shows that land to the south and west of the Waterford releasing bend was uplifted by amounts ranging from 0.4 m to 1.0 m. Land north and east of the Waterford releasing bend subsided by between ~0.4 and 0.8 m. Both subsidence and uplift contributed to the physical expression of scarps on either side of the Waterford releasing bend (Fig. 5B). Maximum subsidence is recorded in a half graben developed on the downthrown side of the West segment, which subsided by at least 0.8 m. However, profile 1 (Fig. 5B), located 2 km east of the Waterford releasing bend, also records 0.4 m of net subsidence. The wide extent of subsidence northeast of the Waterford releasing bend is in keeping with east-west dilation on the West segment due to the dextral slip on the Central segment. Maximum uplift (~1 m) occurred on the south side of the Central segment, east of the Waterford releasing bend (Fig. 5A), while ~0.4 m of uplift occurred on the southwest side of the West segment (profile 3, Fig. 5B).

The vertical displacements revealed by LiDAR difference mapping of the Waterford releasing bend clearly define the strike of the fault and highlight subtle structures that are not otherwise discernible. Most strikingly, LiDAR-determined displacements highlight the overlapping nature of the West and Central segments of the Greendale fault across the Waterford releasing bend. The Greendale fault does not simply curve into a releasing bend, but rather transitions via at least two smaller-scale restraining left steps that are nested within the overall releasing bend. We refer to this nested stepover region, which spans ~800 m, as the "restraining stepover" (Fig. 5A).

The left-stepping minor structures making up the restraining stepover are identified here as CS1 and CS2 (Fig. 5A). The western end of the Central segment strikes 098° and has a well-defined surface scarp ~50 m wide (profile 1, Fig. 5B). About 200 m beyond the western limit of surface deformation on the Central segment, across a restraining bulge defined by uplift contours, is the CS1 structure. The southeastern 300–400 m section of the CS1 structure strikes 120°, but westward, near the edge of the difference map area, it curves back to an east-west strike. The vertical expression of the CS1 structure constitutes a broad (~200 m wide) warp that is ~0.7 m high (profile 2, Fig. 5B). Dextral displacement on CS1 was recorded by Quigley et al. (2012), but vertical displacement on CS1, and its left-stepping relationship to the Central segment, was only determined from the LiDAR data, because the broad, subtle, warping was not visible in the field. About 500 m farther west, there is the north-northwest–striking CS2 structure, which lies approximately subparallel to the Selwyn River. CS2 was not detected in the field. Although the vertical anomaly associated with the CS2 structure is somewhat ambiguous (Fig. 5A), it is clearly revealed by horizontal subpixel correlation of pre- and postearthquake LiDAR rasters (Fig. 5C). Stacked horizontal displacement profiles across CS2 reveal east-west shortening of ~0.8 m (Fig. 5D), due to ~0.6 m of westward motion east of CS2 and ~0.2 m of eastward motion between CS2 and the West segment. The 0.2 m of eastward motion occurred on the northeast side of the West segment.

Although fault-slip planes were not exposed on the Central segment of the Greendale fault, the displacement of the northeast side of the West segment toward the Central segment of the Greendale fault (Fig. 2), coupled with consistent, although slight, uplift to the south of the trace of the Central segment, implies that the Central segment has a southward dip and a minor component of reverse slip. This is in keeping with geodetic modeling by Beavan et al. (Beavan et al., 2010b, 2012). Similarly, the minor structure CS2 is compressional and uplifted to the east, suggesting a component of eastward dip. Together CS1 and CS2 appear to define a positive flower structure.

Apart from the definition of CS2, pixel correlation in this study is generally noisy due to limited extent of the data and few suitable correlation points. Any north-south strike slip on CS2 is lost within this noise and is thus negligible compared with the east-west dip slip. The lack of COSI-Corr evidence for north-south displacements comparable with vertical displacements at the releasing bend suggests that the dip of the Central segment is very steep. CS2 is almost perpendicular to the Central segment, which means that horizontal convergence across CS2 must have been fed by strike slip on the

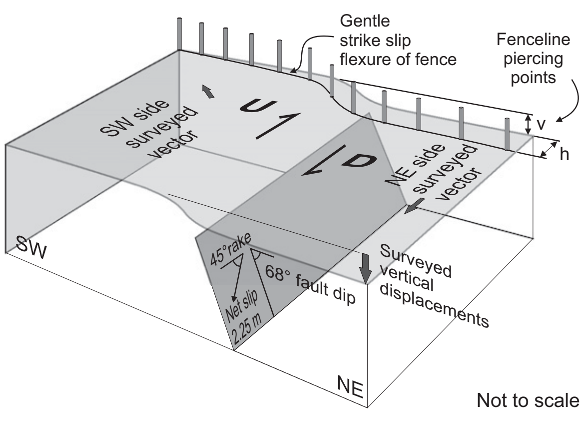

Figure 4. Diagrammatic sketch showing the results of cadastral resurveying and the derivation of net slip across the West segment scarp from the survey data. U and D denote relative upthrow and downthrow across the scarp. The surface "scarp" is a monoclinal flexure of the gravel above the fault plane and is typically at least 20 m wide (see Figs. 3 and 5B). The total width of the strike-slip deformation zone may range up to several hundred meters (see, for example, Villamor et al., 2012). The cadastral survey provides a broader perspective on total displacement and does not depend on long straight linear features (e.g., fence lines) spanning the full width of the deformation zone.

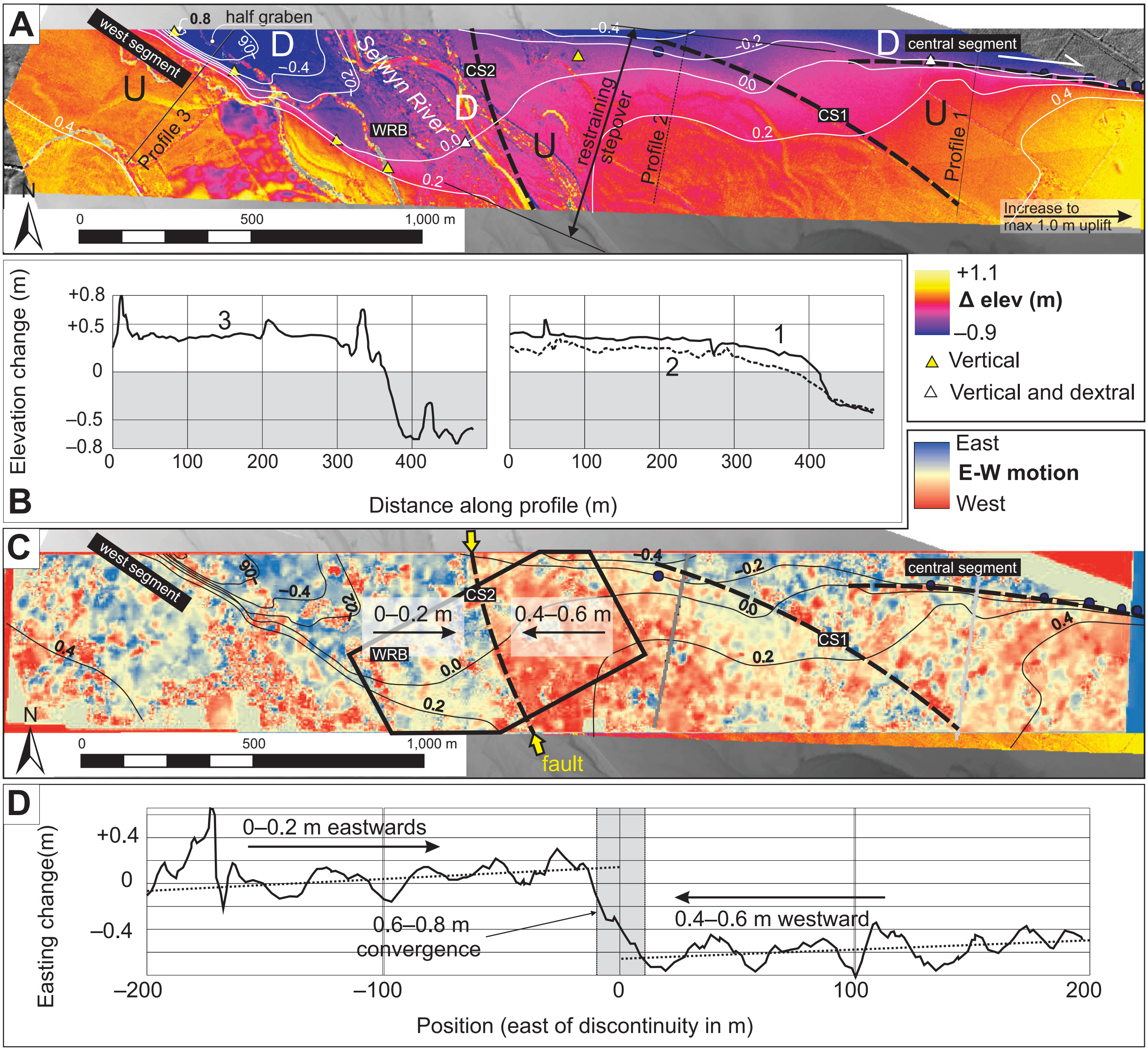

Figure 5. Results of light detection and ranging (LiDAR) differencing. U and D denote relative upthrow and downthrow across the scarp. (A) Post-minus-pre-earthquake LiDAR elevation difference map. White lines are simplified uplift contours (negative values for subsidence). Heavy dashed black lines are faults. Note half-graben development west of the Selwyn River. Selwyn River passes through the surface rupture at a local uplift minimum on the Waterford releasing bend (WRB). (B) Same-scale topographic profiles of fault scarps of the Central segment (CS) (1, 2) and fault scarp of the West segment (3). Gray background indicates net subsidence. For location, see A. Central segment scarps (particularly profile 2) are smaller and more diffuse than the clear scarp on the West segment (profile 3). (C) COSI-Corr subpixel correlation of LiDAR difference model, showing the CS2 structure, along with uplift contours from panel A. The rectangle area was sampled to produce a stacked plot of east-west horizontal displacement (D) that demonstrates 0.6–0.8 m of convergence across the CS2 structure. The gray band denotes the CS2 structure, and the dotted lines represent the mean displacement trends.

Central segment, particularly on CS1. The east-west convergence of 0.8 m across CS2 therefore provides a minimum measure of the strike slip on CS1, which is compatible with the minimum 1.0 ± 0.25 m measured in the field by Quigley et al. (2012) using RTK. By adding a 0.8–1.0 m horizontal displacement to the 0.7 m vertical displacement of CS1 at profile 2, we calculate a minimum net slip of 1.1–1.2 m on CS1. Again, this is compatible with RTK measurements but includes considerably less uncertainty regarding the vertical component of displacement.

In the LiDAR overlap area, the West segment strikes ~122°, which is slightly more westerly than the strike of the fault in the cadastral survey area. The scarp of the West segment, which is clearly defined in the northern part of the difference map (profile 3, Fig. 5B), dies out toward the southeast, ~500 m south of the western end of the Central segment. The Waterford releasing bend between the West and Central segments is a transtensional right bend with respect to strike slip on the Central segment (Fig. 6A[i]), but a contractional left bend with respect to strike slip on the West segment (Fig. 6A[ii]). The east-west shortening on segment CS2 effectively solves the space problem created by transtension on the West segment extending south into the contractional field of CS1 and the Central segment (Fig. 6B).

Displacement Trends

The combination of cadastral and LiDAR mapping techniques clarifies fault displacement trends (Fig. 7). Strike-slip displacements on the West segment increased slightly for 2.5 km southward from the northwestern end of the surface scarp (Fig. 7A) and were generally consistent with, although as much as 25% larger than, the field-survey displacement measurements (Quigley et al., 2012). The discrepancy is probably due in part to the lack of suitably long, originally straight markers crossing this sector of the fault zone, and in part to the survey marks reflecting the overall effects of larger displacements at depth (e.g., Beavan et al., 2010b).

Southeast of the cadastral survey area, strike-slip displacements determined by LiDAR differencing decline over a distance of 2.5 km, from 1.5 m to approximately zero at the Waterford releasing bend, where only 0.2 m of eastward horizontal motion of the hanging wall is calculated from pixel correlation at the restraining stepover to the Central segment (Fig. 5D). Strike-slip displacements increase east of Waterford releasing bend. A single estimate of 0.8 m of dextral displacement at the location of profile 2 (Fig. 5) is consistent with previously obtained at-fault displacement measurements (Quigley et al., 2012).

The net vertical displacement also declines in the area of the restraining stepover (Fig. 7B). Relative vertical displacements in the cadastral survey area range from 1.4 to 1.6 m. Within the LiDAR map area, the vertical displacements on the West segment immediately northwest of the restraining stepover totaled ~1.2 m, ~25% less than the 1.4–1.6 m vertical displacements across the cadastral survey network. These data show a consistent reduction in vertical displacement south toward the Waterford releasing bend and its restraining stepover (Fig. 7B). This pattern of decreasing displacement is associated with dying out of a half graben that is highlighted by vertical displacement contours northwest of the Waterford releasing bend (Fig. 5A).

The 2.25 m of net slip calculated using our cadastral-based vertical and strike-slip determinations on the West segment is more than double the 1 m of net slip estimated close to the Waterford releasing bend at profile 2 (Fig. 5A). The reduced displacement toward the Waterford releasing bend coincides with increasingly diffuse and subtle scarp expression. Away from the Waterford releasing bend, within our study area, the scarp on both segments is well defined (≤50 m wide; Fig. 5B, profiles 1 and 3). Closer to the Waterford releasing bend, the scarp becomes diffuse, and elevation change is distributed across 200–300 m (e.g., profile 2, Figs. 5A and 5B). Between CS2 and the West segment, the uplift gradient declines to only around 0.2%, and no scarp is definable. The Selwyn River, either fortuitously or due to structural control (as inferred for the nearby Hawkins River by Campbell et al., 2012), crosses the fault trace at this local minimum in vertical displacement (Figs. 5A and 7), and exhibits a reduction of its bed gradient of only <0.1% over 600 m. The slight reduction in bed gradient, coupled with a 0.2% tilt toward the fault imposed by the half graben, may increase the flood hazard in the vicinity of the fault.

DISCUSSION

The processes governing fault-rupture behavior at releasing bends are not well understood (Cunningham and Mann, 2007; Mann, 2007), in part because surface rupture at a fault bend is commonly subtle and/or distributed (King and Nábělek, 1985; King, 1986; Devès et al., 2011). Accurate, high-resolution documentation of surface displacement provides an important piece of information on fault characteristics in these zones. This study has illuminated the dis-

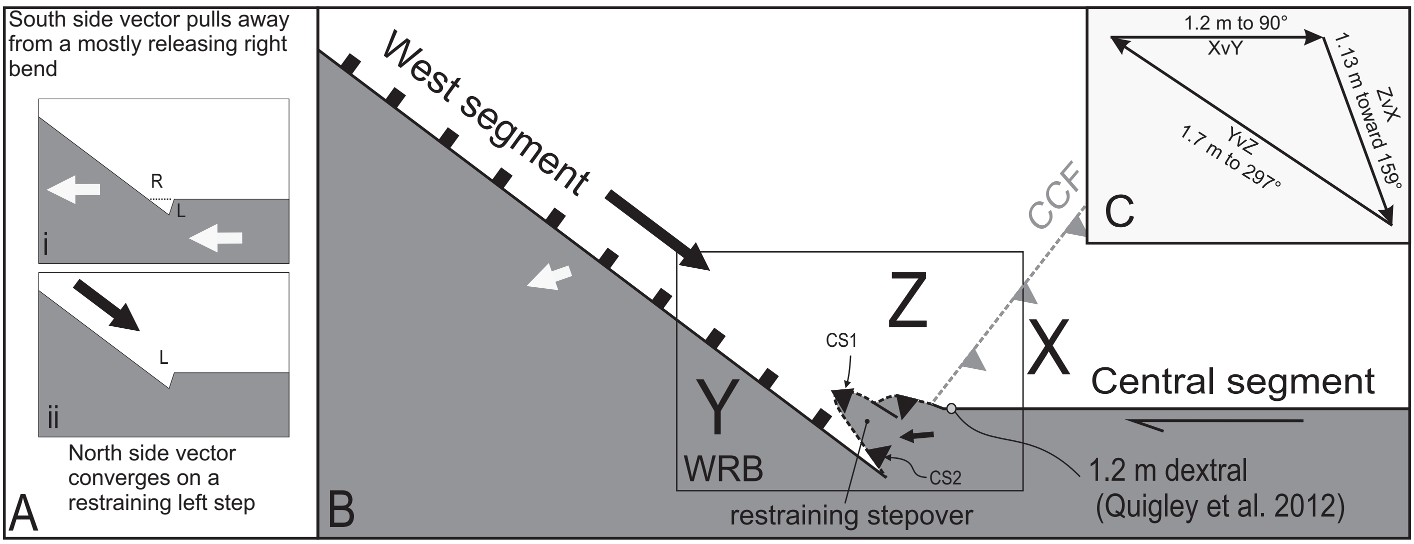

Figure 6. Structures contributing to the development of the Waterford releasing bend (WRB) area. (A) Sketch maps of the bend from the perspectives of surface displacement vectors on the south (i) and north sides of the fault (ii). L and R indicate left and right bends or steps. (B) The net result of combining the two sets of structures. CCF—location of subsurface tip of blind Charing Cross fault. The westward-directed south-side vector dilates the West segment. The minor left bend onto the overlapping southern tip of the West segment is accommodated by CS2. Convergence of the north-side vector with the Central segment is expressed by the nested restraining stepover onto CS1, and accommodated at a larger scale by underplating at the footwall of the CCF. (C) Vector calculation for relative horizontal displacement across the Charing Cross fault based on Equation 1, assuming a triple junction between the West and Central segments and the Charing Cross fault.

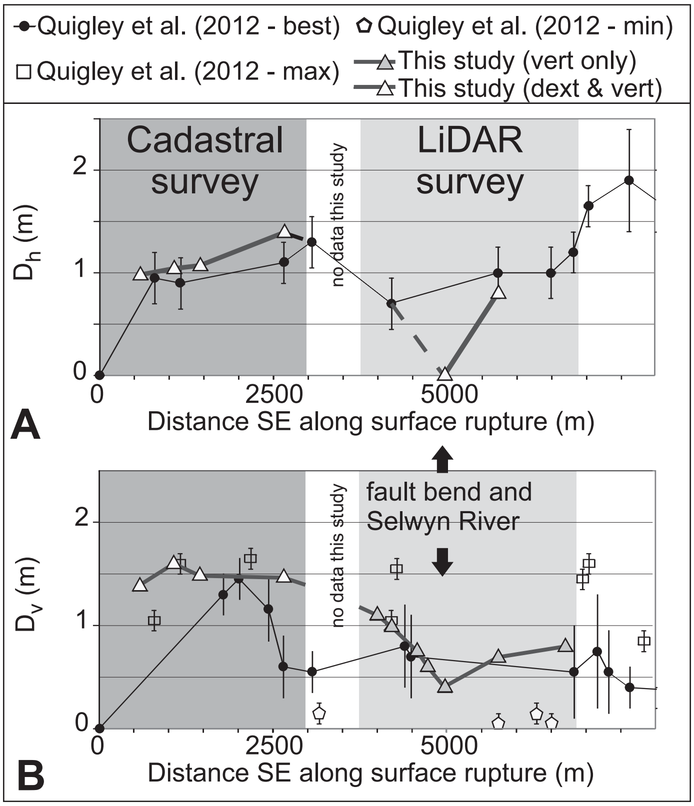

Figure 7. Displacement trends on the West and Central segments in the vicinity of the Waterford releasing bend. (A) Dextral and (B) vertical displacement plots for the bend area comparing data of Quigley et al. (2012; field mapping) and this study. Note the displacement minimum at the Waterford releasing bend at distance 5000 m. LiDAR—light detection and ranging.

placement interrelationships that arose across a releasing bend between the West and Central segments of the Greendale fault during a single, surface-rupturing, multifault earthquake. The deformation at the Waterford releasing bend is particularly subtle. We have shown that field-based fault mapping was only able to identify the main scarps of the West and Central segments, but no deformation was detected in the releasing bend area. Furthermore, this area lay in an ~1.5-m-wide low-coherence zone in the differential InSAR data (Beavan et al., 2010b; Elliott et al., 2012), and therefore the InSAR could not quantify the nature of deformation across the Waterford releasing bend. Because the postearthquake LiDAR was flown prior to mapping of the West segment, and thus did not cover that segment, the mapping of fault-induced avulsion flooding provided a useful asset that was instrumental in helping define the location and geometry of the West segment and Waterford releasing bend.

The vertical displacements shown by LiDAR on the West segment near the Waterford releasing bend are greater than Beavan et al.'s (2010b) values, in terms of both maximum uplift (0.4 compared to 0.1 m) and maximum subsidence (0.8 compared to 0.6 m). The total vertical displacements in the cadastral survey area along the West segment of the Greendale fault are even greater but cannot be stated in terms of absolute uplift and subsidence. The greater uplift and subsidence at the West segment, compared with the far-field values, suggest that the footwall of the West segment is a southwest-tilted uplifted block and that the hanging wall is downwarped into a half graben close to fault. This is consistent with elastic rebound on a normal fault (Koseluk and Bischke, 1981) or with a near-surface steepening of fault dip (Bray et al., 1994).

Surface displacement on the Greendale fault reaches a minimum at the Waterford releasing bend, and increases either side of the bend. This is consistent with predictions of slip distribution at the intersection of two separate, differently oriented, same-sense fault zones (King and Nábělek, 1985). Changes in the orientation of strike-slip faults that cause local extension or contraction on continuously curved bounding faults are typically referred to as releasing and restraining bends, respectively. On the other hand, stepovers commonly transfer slip between separate, subparallel, overlapping faults (e.g., Christie-Blick and Biddle, 1985). The combination of investigation techniques shows that the Waterford releasing bend, which appeared at first glance to be a simple curve in a single strike-slip fault (e.g., Sibson et al., 2011), marks a complicated transition from a steeply south-dipping strike-slip fault (Central segment) to an overlapping, northwest-dipping, dextral transtensional fault (West segment) (Fig. 5). The transition incorporates elements of bend as well as stepover geometry.

Compared with regional geodetic surveys (Beavan et al., 2010b, 2012; Elliott et al., 2012), our data provide improved constraints on the displacements that occurred within an area where the InSAR decorrelated and where there were few high-order trigonometric points for GPS surveys. The horizontal displacements and the net slip estimates from the cadastral survey detailed here are consistent with those of Beavan et al. (2010b) in azimuth and magnitude, and the GPS horizontal displacements measured by Beavan for the cadastral part of this study are incorporated in the model of Beavan et al. (2012). Our determination of net slip of 2.25 m is greater than the near-surface value of 1.5 m calculated by Elliott et al. (2012) from InSAR but consistent with their modeled slip at 1–2 km depth.

Our calculated movement vectors show that the south and southwest side of the Greendale fault shifted westward as a coherent block. Therefore, seen from the south side of the fault, the Waterford releasing bend is indeed a transtensional right bend (Fig. 6A[i]). However, the southeastern 500 m section of the West segment is in a contractional quadrant for the Central segment. In this context, the east-west contraction across the CS2 component of the restraining stepover (Fig. 5D) accommodates this convergence (Figs. 6A[i] and 6B).

Movement vectors on the north and northeast side of the Greendale fault are toward the east-southeast, parallel to the West segment, and thus movement of the north side of the West segment converged toward a restraining left step onto the Central segment (Fig. 6A[ii]). The restraining step is nested in the overall releasing bend (Fig. 6B) and is at least 800 m wide, similar to the width of the restraining stepover that separates the Central and East Greendale fault segments (Quigley et al., 2012).

Restraint of strike slip on the West segment is one way of kinematically reconciling the restraining stepover nested within the Waterford releasing bend. However, the blind Charing Cross fault, on which the rupture sequence initiated, forms a triple junction with the Central and West segments and therefore may have had a role to play in the coseismic geometric relationships expressed in and around the Waterford releasing bend. For a triple junction to remain stable, the relative motion vectors at the triple junction should sum to zero, such that

$$ {}_{X}V_{Y} + {}_{Y}V_{Z} + {}_{Z}V_{X} = 0, \qquad (1) $$

where ${}_{X}V_{Y}$ is the motion of block Y relative to block X (Fig. 6C). The Charing Cross fault is blind, so the exact location of its intersection with the Central and West segments is unclear. However, the best available estimate is provided by the surface projection shown by Beavan et al. (2012), lying just outside the differential LiDAR (see Fig. 2). Based on that location, block Y, which lies south of the Central segment and southwest of the West segment (Fig. 6), moved 1.2 m west relative to the southeastern side (hanging wall) of the Charing Cross fault (block X on Fig. 6) (Quigley et al., 2012), and ~1.7 m northwest relative to block Z, which is the footwall of the Charing Cross fault (and also the hanging wall of the West segment). By Equation 1, horizontal convergence across the Charing Cross fault was therefore ~1.13 m toward 159° (Fig. 6C). A northwest-striking sinistral strike-slip fault of this orientation is inferred to form the northern termination of the Charing Cross fault (Beavan et al., 2012; Elliott et al., 2012) (Fig. 1B). It was suggested by both Beavan et al. (2012) and Elliott et al. (2012) that the northwest-striking, opposite-sense, strike-slip faults at either end of the Charing Cross fault acted as transfer structures, between which rock was fed toward the Charing Cross fault. Therefore, slip on the Charing Cross fault consisted of underplating of what, moments later, was to become the hanging-wall block of the West segment. Contraction on the Charing Cross fault may have contributed to ground-surface deformation in the area of the Waterford releasing bend.

Fault complexities such as bends and stepovers are widely recognized to be important factors in rupture arrest (Wesnousky, 2006). Studies such as those by Elliott et al. (2009) and Ben-Zion et al. (2012) suggest that bend complexities may influence and even control dynamic rupture behavior, and those authors set out to develop geomorphic and structural parameters to aid prediction of rupture arrest at smaller bends and stepovers. Much larger pop-up structures, the collective expression of numerous rupture events, have been identified nested in equivalent positions at releasing transfer zones on several Californian faults, including the stepover between the San Andreas and Imperial faults (Ben-Zion et al., 2012). Ben Zion et al. postulated that such structures are likely locations of rupture segmentation. Similar subtle structures developed in bedrock during the Duzce earthquake at the Lake Eften releasing double bend (Duman et al., 2005, their Fig. 3), which formed an overlap segment that ruptured during both the Izmit and Duzce earthquakes (Hartleb et al., 2002; Akyüz et al., 2002; Konca et al., 2010). Dextral slip on the Totschunda fault during the Denali earthquake (Eberhart-Phillips et al., 2003) would almost certainly have created similar structures at the intersection with the Denali fault. However, the types of structures that we detected at the Waterford releasing bend, which are subtle but fundamental surface expressions of fault kinematics, are commonly indiscernible at single rupture displacement scales and particularly in alluvial settings. At the Waterford releasing bend on the Greendale fault, the observations of subtle deformation and the location of the nested restraining stepover in an active alluvial setting suggest that the preservation of these specific structures will be short-lived in the local geologic-geomorphic record. Nevertheless, we have been able to extract a very valuable single-event deformation record that is unencumbered by topographic features related to previous events. Similar data sets are likely to emerge from initiatives such as GeoEarthScope LiDAR acquisition in California (Prentice et al., 2009). Such data sets are expected to provide detailed insights into fault complexity and kinematic interactions and should contribute greatly to modeling and field testing of hypotheses regarding the influences of fault bends and stepovers on the terminations of earthquake ruptures (Elliott et al., 2009; Ben-Zion et al., 2012).

CONCLUSIONS

Spatial and temporal overlap of a number of high-quality data sets, including pre- and post-earthquake LiDAR, cadastral survey data, fault-rupture mapping, and displaced piercing points (e.g., straight fences and the like), has allowed remarkably high-resolution documentation of the kinematics and fault interactions at a releasing fault bend. The measurements confirm that the West segment of the Greendale fault is a separate, northwest-striking dextral-oblique normal fault that released dextral motion on the Central segment of the Greendale fault, across what is broadly speaking a releasing bend. In detail, an ~800-m-wide zone of left-stepping restraining stepovers lies nested within the overall releasing bend. Cadastral survey data allowed determination of net slip on the West segment, which, at 2.25 m, is substantially higher than previously estimated from piercing point measurements. This displacement decreases to near zero at the restraining stepover. The clear documentation and characterization of deformation and structure at this releasing bend provide insight into subtle, but potentially important, structures and issues that may be present at bends on strike-slip faults elsewhere.

ACKNOWLEDGMENTS

This study was funded by the Department of Geological Sciences, University of Canterbury, and by the New Zealand Earthquake Commission (EQC). B. Duffy was supported by a New Zealand Tertiary Education Commission Top Achiever Scholarship. S. Leprince was partly supported by the Keck Institute for Space Studies and by the Gordon and Betty Moore Foundation. We thank J. Beavan for global positioning system survey data, landowners for field access, N. Carson, J. Campbell, S. Hornblow, and A. Mackenzie for field assistance, and Environment Canterbury for LiDAR data. We are grateful to Timothy Little, Paul Mann, John Walsh, James Dolan, and Richard Norris for thoughtful reviews that greatly improved the manuscript.

REFERENCES CITED

Akyüz, H.S., Hartleb, R., Barka, A., Altunel, E., Sunal, G., Meyer, B., and Armijo, R., 2002, Surface Rupture and Slip Distribution of the 12 November 1999 Düzce Earthquake (M 7.1), North Anatolian Fault, Bolu, Turkey: Bulletin of the Seismological Society of America, v. 92, p. 61–66, doi:10.1785/0120000840.

Barrell, D.J.A., Litchfield, N.J., Townsend, D.B., Quigley, M.C., Van Dissen, R.J., Cox, S.C., Cosgrove, R., Furlong, K., Villamor, P., Begg, J.G., Hemmings-Sykes, S., Jongens, R., Mackenzie, H., Stahl, T., Bilderback, E., Duffy, B., Lang, E.M.W., Nicol, R., Noble, D., and Pedley, K., 2011, Strike-slip ground-surface rupture (Greendale fault) associated with the 4 September 2010 Darfield earthquake, Canterbury, New Zealand: Quarterly Journal of Engineering Geology and Hydrogeology, v. 44, p. 283–291, doi:10.1144/1470-9236/11-034.

Beavan, J., Samsonov, S., Denys, P., Sutherland, R., Palmer, N., and Denham, M., 2010a, Oblique slip on the Puysegur subduction interface in the 2009 July M_W 7.8 Dusky Sound earthquake from GPS and InSAR observations: Implications for the tectonics of southwestern New Zealand: Geophysical Journal International, v. 183, no. 3, p. 1265–1286, doi:10.1111/j.1365-246X.2010.04798.x.

Beavan, J., Samsonov, S., Motagh, M., Wallace, L.M., Ellis, S.M., and Palmer, N., 2010b, The Darfield (Canterbury) earthquake: Geodetic observations and preliminary source model: Bulletin of the New Zealand Society for Earthquake Engineering, v. 43, no. 4, p. 228–235.

Beavan, J., Motagh, M., Fielding, E., Donnelly, N., and Collett, D., 2012, Fault slip models of the 2010–2011 Canterbury, New Zealand, earthquakes from geodetic data, and observations of post-seismic ground deformation: New Zealand Journal of Geology and Geophysics (Special issue: Canterbury, New Zealand, 2010–2011 earthquake sequence), v. 55, no. 3, p. 207–221.

Ben-Zion, Y., Rockwell, T.K., Shi, Z., and Xu, S., 2012, Reversed-polarity secondary deformation structures near fault stepovers: Journal of Applied Mechanics, v. 79, no. 3, p. 031025, doi:10.1115/1.4006154.

Bowditch, N., 1808, The first method to adjust a traverse based on statistical considerations: The Analyst or Mathematical Museum, v. 1, no. 2, p. 42.

Bray, J., Seed, R., Cluff, L., and Seed, H., 1994, Earthquake fault rupture propagation through soil: Journal of Geotechnical Engineering, v. 120, no. 3, p. 543–561, doi: 10.1061/(ASCE)0733-9410(1994)120:3(543).

Browne, G.H., Field, B.D., Barrell, D.J.A., Jongens, R., Bassett, K.N., and Wood, R.A., 2012, The geological setting of the Darfield and Christchurch earthquakes: New Zealand Journal of Geology and Geophysics (Special issue: Canterbury, New Zealand, 2010–2011 earthquake sequence), v. 55, no. 3, p. 193–197.

Campbell, J., Pettinga, J., and Jongens, R., 2012, The tectonic and structural setting of the 4th September 2010 Darfield (Canterbury) earthquake sequence, New Zealand: New Zealand Journal of Geology and Geophysics (Special issue: Canterbury, New Zealand, 2010–2011 earthquake sequence), v. 55, no. 3, p. 155–168.

Christie-Blick, N., and Biddle, K.T., 1985, Deformation and basin formation along strike slip faults, *in* Biddle, K.T., and Christie-Blick, N., eds., Strike-Slip Deformation, Basin Formation, and Sedimentation: Tulsa, Oklahoma, Society of Economic Paleontologists and Mineralogists, p. 1–34.

Cox, S.C., and Barrell, D.J.A., 2007, Geology of the Aoraki Area: Institute of Geological and Nuclear Sciences Geological Map 15: Lower Hutt, New Zealand, GNS Science, scale 1:250,000, 1 sheet and 71 p.

Cox, S.C., Rutter, H.J., Sims, A., Mangad, M., Weir, J.J., Ezzy, T., White, P.A., Horton, T.W., and Scott, D., 2012, Hydrological effects of the M_W7.1 Darfield (Canterbury) earthquake, 4 September 2010, New Zealand: New Zealand Journal of Geology and Geophysics (Special issue: Canterbury, New Zealand, 2010–2011 earthquake sequence), v. 55, no. 3, p. 231–247.

Cubrinovski, M., Green, R.A., Allen, J., Ashford, S., Bowman, E., Bradley, B., Cox, B., Hutchinson, T., Kavazanjian, E., Orense, R., Pender, M., Quigley, M.C., and Wotherspoon, L., 2010, Geotechnical reconnaissance of the 2010 Darfield (Canterbury) earthquake: Bulletin of the New Zealand Society for Earthquake Engineering, v. 43, no. 4, p. 243–320.

Cunningham, W.D., and Mann, P., 2007, Tectonics of strike-slip restraining and releasing bends, *in* Cunningham, D., and Mann, P., eds., Tectonics of Strike-Slip Restraining and Releasing Bends: Geological Society of London Special Publication 290, p. 1–12.

DeMets, C., Gordon, R.G., and Argus, D.F., 2010, Geologically current plate motions: Geophysical Journal International, v. 181, no. 1, p. 1–80, doi:10.1111/j.1365-246X.2009.04491.x.

Devès, M., King, G.C.P., Klinger, Y., and Agnon, A., 2011, Localised and distributed deformation in the lithosphere: Modelling the Dead Sea region in 3 dimensions: Earth and Planetary Science Letters, v. 308, no. 1–2, p. 172–184, doi:10.1016/j.epsl.2011.05.044.

Duman, T.Y., Emre, O., Dogan, A., and Ozalp, S., 2005, Step-over and bend structures along the 1999 Duzce earthquake surface rupture, North Anatolian fault, Turkey: Bulletin of the Seismological Society of America, v. 95, no. 4, p. 1250–1262, doi:10.1785/0120040082.

Eberhart-Phillips, D., Haeussler, P.J., Freymueller, J.T., Frankel, A.D., Rubin, C.M., Craw, P., Ratchkovski, N.A., Anderson, G., Carver, G.A., Crone, A.J., Dawson, T.E., Fletcher, H., Hansen, R., Harp, E.L., Harris, R.A., Hill, D.P., Hreinsdóttir, S., Jibson, R.W., Jones, L.M., Kayen, R., Keefer, D.K., Larsen, C.F., Moran, S.C., Personius, S.F., Plafker, G., Sherrod, B., Sieh, K., Sitar, N., and Wallace, W.K., 2003, The 2002 Denali fault earthquake, Alaska: A large magnitude, slip-partitioned event: Science, v. 300, no. 5622, p. 1113–1118, doi:10.1126/science.1082703.

Elliott, A.J., Dolan, J.F., and Oglesby, D.D., 2009, Evidence from coseismic slip gradients for dynamic control on rupture propagation and arrest through stepovers: Journal of Geophysical Research–Solid Earth, v. 114, no. B2, B02313, doi:10.1029/2008JB005969.

Elliott, J.R., Nissen, E.K., England, P.C., Jackson, J.A., Lamb, S., Li, Z., Oehlers, M., and Parsons, B., 2012, Slip in the 2010 and 2011 Canterbury earthquakes, New Zealand: Journal of Geophysical Research, v. 117, no. B3, B03401, doi:10.1029/2011JB008868.

Forsyth, P.J., Barrell, D.J.A., and Jongens, R., 2008, Geology of the Christchurch Area: Institute of Geological and Nuclear Sciences Geological Map 16: Lower Hutt, New Zealand, GNS Science, 1 sheet + 67 p., scale 1:250,000.

Gledhill, K., Ristau, J., Reyners, M., Fry, B., Holden, C., and GeoNet-Team, 2010, The Darfield (Canterbury) earthquake of September 2010: Preliminary seismological report: Bulletin of the New Zealand Society for Earthquake Engineering, v. 43, no. 4, p. 215–221.

Gledhill, K., Ristau, J., Reyners, M., Fry, B., and Holden, C., 2011, The Darfield (Canterbury, New Zealand) Mw 7.1 earthquake of September 2010: A preliminary seismological report: Seismological Research Letters, v. 82, p. 378–386, doi:10.1785/gssrl.82.3.378.

Hartleb, R.D., Dolan, J.F., Akyüz, H.S., Dawson, T.E., Tucker, A.Z., Yerli, B., Rockwell, T.K., Toraman, E., Çakir, Z., Dikba, A., and Altunel, E., 2002, Surface rupture and slip distribution along the Karadere segment of the 17 August 1999 İzmit and the western section of the 12 November 1999 Düzce, Turkey, earthquakes: Bulletin of the Seismological Society of America, v. 92, no. 1, p. 67–78, doi:10.1785/0120000829.

Holden, C., Beavan, J., Fry, B., Reyners, M., Ristau, J., Van Dissen, R., Villamor, P., and Quigley, M., 2011, Preliminary source model of the M_W 7.1 Darfield earthquake from geological, geodetic and seismic data, *in* Proceedings of the Ninth Pacific Conference on Earthquake Engineering, Building an Earthquake-Resilient Society, 14–16 April 2011, Auckland, New Zealand: New Zealand Society for Earthquake Engineering, Paper 164, 7 p.

Hudnut, K.W., Borsa, A., Glennie, C., and Minster, J.-B., 2002, High-resolution topography along surface rupture of the 16 October 1999 Hector Mine, California, earthquake (M_W 7.1) from airborne laser swath mapping: Bulletin of the Seismological Society of America, v. 92, no. 4, p. 1570–1576, doi:10.1785/0120000934.

Jongens, R., Barrell, D.J.A., Campbell, J.K., and Pettinga, J.R., 2012, Faulting and folding beneath the Canterbury Plains identified prior to the 2010 emergence of the Greendale fault: New Zealand Journal of Geology and Geophysics (Special issue: Canterbury, New Zealand, 2010–2011 earthquake sequence), v. 55, no. 3, p. 169–176.

King, G., and Nábělek, J., 1985, Role of fault bends in the initiation and termination of earthquake rupture: Science, v. 228, no. 4702, p. 984–987, doi:10.1126/science.228.4702.984.

King, G.C.P., 1986, Speculations on the geometry of the initiation and termination processes of earthquake rupture and its relation to morphology and geological structure: Pure and Applied Geophysics, v. 124, no. 3, p. 567–585, doi:10.1007/BF00877216.

Konca, A.O., Leprince, S., Avouac, J.P., and Helmberger, D.V., 2010, Rupture process of the 1999 M_W 7.1 Duzce earthquake from joint analysis of SPOT, GPS, InSAR, strong-motion, and teleseismic data: A supershear rupture with variable rupture velocity: Bulletin of the Seismological Society of America, v. 100, no. 1, p. 267–288, doi:10.1785/0120090072.

Koseluk, R.A., and Bischke, R.E., 1981, An elastic rebound model for normal fault earthquakes: Journal of Geophysical Research, v. 86, no. B2, p. 1081–1090, doi:10.1029/JB086iB02p01081.

Lee, Y.H., Chen, H.S., Rau, R.J., Chen, C.L., and Hung, P.S., 2006, Revealing surface deformation of the 1999 Chi-Chi earthquake using high-density cadastral control points in the Taichung area, central Taiwan: Bulletin of the Seismological Society of America, v. 96, no. 6, p. 2431–2440, doi:10.1785/0120060055.

Lee, Y.H., Wu, K.C., Rau, R.J., Chen, H.C., Lo, W., and Cheng, K.C., 2010, Revealing coseismic displacements and the deformation zones of the 1999 Chi-Chi earthquake in the Tsaotung area, central Taiwan, using digital cadastral data: Journal of Geophysical Research–Solid Earth, v. 115, B03419, 13 p.

Lee, Y.H., Chen, Y.C., Chen, C.L., Rau, R.J., Chen, H.C., Lo, W., and Cheng, K.C., 2011, Revealing coseismic displacement and displacement partitioning at the northern end of the 1999 Chi-Chi earthquake, central Taiwan, using digital cadastral data: Bulletin of the Seismological Society of America, v. 101, no. 3, p. 1199–1212, doi:10.1785/0120100156.

Leprince, S., Ayoub, F., Klinger, Y., and Avouac, J.P., 2007a, Co-registration of optically sensed images and correlation (COSI-Corr): An operational methodology for ground deformation measurements, *in* Proceedings of the IEEE International Geoscience and Remote Sensing Symposium (IGARSS 2007), Barcelona, Spain, p. 1943–1946.

Leprince, S., Barbot, S., Ayoub, F., and Avouac, J. P., 2007b, Automatic and precise ortho-rectification, coregistration, and subpixel correlation of satellite images: Application to ground deformation measurements: IEEE Transactions on Geoscience and Remote Sensing, v. 45, p. 1529–1558.

Mann, P., 2007, Global catalogue, classification and tectonic origins of restraining and releasing bends on active and ancient strike-slip fault systems, *in* Cunningham, D., and Mann, P., eds., Tectonics of Strike-Slip Restraining and Releasing Bends: Geological Society of London Special Publication 290, p. 13–142.

Marsella, M., Proietti, C., Sonnessa, A., Coltelli, M., Tommasi, P., and Bernardo, E., 2009, The evolution of the Sciara del Fuoco subaerial slope during the 2007 Stromboli eruption: Relation between deformation processes and effusive activity: Journal of Volcanology and Geothermal Research, v. 182, no. 3–4, p. 201–213, doi:10.1016/j.jvolgeores.2009.02.002.

Mukoyama, S., 2011, Estimation of ground deformation caused by the earthquake (M7.2) in Japan, 2008, from the geomorphic image analysis of high resolution LiDAR DEMs: Journal of Mountain Science, v. 8, no. 2, p. 239–245, doi:10.1007/s11629-011-2106-7.

Muller, J.R., and Harding, D.J., 2007, Using LIDAR surface deformation mapping to constrain earthquake magnitudes on the Seattle fault in Washington State, USA, *in* Proceedings of the Urban Remote Sensing Joint Event, 11–13 April 2007: Institute of Electrical and Electronics Engineers (IEEE), p. 1–7, doi:10.1109/URS.2007.371789.

Norris, R.J., and Cooper, A.F., 2001, Late Quaternary slip rates and slip partitioning on the Alpine fault, New Zealand: Journal of Structural Geology, v. 23, no. 2–3, p. 507–520, doi:10.1016/S0191-8141(00)00122-X.

Oskin, M.E., Arrowsmith, J.R., Corona, A.H., Elliott, A.J., Fletcher, J.M., Fielding, E.J., Gold, P.O., Garcia, J.J.G., Hudnut, K.W., Liu-Zeng, J., and Teran, O.J., 2012, Near-field deformation from the El Mayor–Cucapah earthquake revealed by differential LIDAR: Science, v. 335, p. 702–705, doi:10.1126/science.1213778.

Pettinga, J.R., Yetton, M.D., Van Dissen, R.J., and Downes, G., 2001, Earthquake source identification and characterisation for the Canterbury region, South Island, New Zealand: Bulletin of the New Zealand Society for Earthquake Engineering, v. 34, no. 4, p. 282–317.

Prentice, C.S., Crosby, C.J., Whitehill, C.S., Arrowsmith, J.R., Furlong, K.P., and Phillips, D.A., 2009, Illuminating Northern California's active faults: Eos (Transactions, American Geophysical Union), v. 90, no. 7, p. 55, doi:10.1029/2009EO070002.

Price, E.J., and Burgmann, R., 2002, Interactions between the Landers and Hector Mine, California, earthquakes from space geodesy, boundary element modeling, and time-dependent friction: Bulletin of the Seismological Society of America, v. 92, no. 4, p. 1450–1469, doi:10.1785/0120000924.

Quigley, M.C., Van Dissen, R., Villamor, P., Litchfield, N., Barrell, D., Furlong, K., Stahl, T., Duffy, B., Bilderback, E., Noble, D., Townsend, D., Begg, J., Jongens, R., Ries, W., Claridge, J., Klahn, A., Mackenzie, H., Smith, A., Hornblow, S., Nicol, R., Cox, S., Langridge, R., and Pedley, K., 2010a, Surface rupture of the Greendale fault during the Darfield (Canterbury) earthquake, New Zealand: Initial findings: Bulletin of the New Zealand Society for Earthquake Engineering, v. 43, no. 4, p. 236–242.

Quigley, M.C., Villamor, P., Furlong, K., Beavan, J., Van Dissen, R., Litchfield, N., Stahl, T., Duffy, B., Bilderback, E., Noble, D., Barrell, D., Jongens, R., and Cox, S., 2010b, Previously unknown fault shakes New Zealand's South Island: Eos (Transactions, American Geophysical Union), v. 91, no. 49, p. 469–470, doi:10.1029/2010EO490001.

Quigley, M.C., Van Dissen, R., Litchfield, N., Villamor, P., Duffy, B., Barrell, D., Furlong, K., Stahl, T., Bilderback, E., and Noble, D., 2012, Surface rupture during the 2010 M_W 7.1 Darfield (Canterbury) earthquake: Implications for fault rupture dynamics and seismic-hazard analysis: Geology, v. 40, no. 1, p. 55–58, doi:10.1130/G32528.1.

Quigley, M.C., Bastin, S., and Bradley, B., 2013, Recurrent liquefaction in Christchurch, New Zealand, during the Canterbury earthquake sequence: Geology, doi:10.1130/G33944.1 (in press).

Reigber, C., Xia, Y., Michel, G.W., Klotz, J., and Angermann, D., 1997, The Antofagasta 1995 earthquake: Crustal deformation pattern as observed by GPS and D-INSAR, *in* Proceedings of the Third ERS Symposium on Space at the Service of Our Environment, 14–21 March 1997, Florence, Italy: European Space Agency, p. 507–513.

Sibson, R., Ghisetti, F., and Ristau, J., 2011, Stress control of an evolving strike-slip fault system during the 2010–2011 Canterbury, New Zealand, earthquake sequence: Seismological Research Letters, v. 82, no. 6, p. 824–832, doi:10.1785/gssrl.82.6.824.

Van Dissen, R., Barrell, D., Litchfield, N., King, A., Quigley, M., Villamor, P., Furlong, K., Mackenzie, H., Klahn, A., Begg, J., Townsend, D., Stahl, T., Noble, D., Duffy, B., Bilderback, E., Jongens, R., Cox, S., Langridge, R., Ries, W., Dhakal, R., Smith, A., Nicol, R., Pedley, K., Henham, H., and Hunter, R., 2011, Surface rupture displacement on the Greendale fault during the Mw 7.1 Darfield (Canterbury) earthquake, New Zealand, and its impact on man-made structures, *in* Proceedings Ninth Pacific Conference on Earthquake Engineering, Building an Earthquake-Resilient Society, Auckland, New Zealand, 14–16 April 2011: New Zealand Society for Earthquake Engineering, Paper 186, 8 p.

Villamor, P., Litchfield, N., Barrell, D., Van Dissen, R., Hornblow, S., Quigley, M., Levick, S., Ries, W., Duffy, B., Begg, J., Townsend, D., Stahl, T., Bilderback, E., Noble, D., Furlong, K., and Grant, H., 2012, Map of the 2010 Greendale fault surface rupture, Canterbury, New Zealand: Application to land use planning: New Zealand Journal of Geology and Geophysics (Special issue: Canterbury, New Zealand, 2010–2011 earthquake sequence), v. 55, no. 3, p. 223–330.

Wesnousky, S.G., 2006, Predicting the endpoints of earthquake ruptures: Nature, v. 444, no. 7117, p. 358–360, doi:10.1038/nature05275.

Science Editor: Nancy Riggs
Associate Editor: J.J. Walsh

Manuscript Received 24 June 2012
Revised Manuscript Received 21 October 2012
Manuscript Accepted 7 November 2012

Printed in the USA